



Article

Shadow Cast of Rotating Charged Black Hole with Scalar Q-Hair

Meng-He Wu ^{1,2} , Hong Guo ³  and Xiao-Mei Kuang ^{4,*}

¹ School of Mathematics, Physics and Statistics, Shanghai University of Engineering Science, Shanghai 201620, China

² Center of Application and Research of Computational Physics, Shanghai University of Engineering Science, Shanghai 201620, China

³ School of Physics and Astronomy, Shanghai Jiao Tong University, Shanghai 200240, China

⁴ Center for Gravitation and Cosmology, College of Physical Science and Technology, Yangzhou University, Yangzhou 225002, China

* Correspondence: xmeikuang@yzu.edu.cn

Abstract: In this paper, we investigate the shadow cast by non-rotating and rotating charged black holes with scalar Q-hair. We find that in addition to the spin parameter of black hole and inclination angle of the observer, the charge parameter and the self-interaction parameters of the scalar hair also influence the shape of the black hole shadow. Our studies show that the charged black holes with scalar Q-hair always have smaller shadow size compared to those without hair. Moreover, it is found that the parameters significantly affect the shadow observables. In particular, for the fixed spin parameter and inclination angle, a larger charge parameter will increase the shadow size but decrease the shadow distortion, whilst stronger self-interaction parameters have the opposite influence. In short, the shadow of the charged black hole with scalar Q-hair can be distinguished from the Reissner–Nordström (RN) black hole or Kerr–Newmann (KN) black hole, and they indeed generate new templates with large deviations from general relativity those are invariably smaller in size.



Citation: Wu, M.-H.; Guo, H.; Kuang, X.-M. Shadow Cast of Rotating Charged Black Hole with Scalar Q-Hair. *Symmetry* **2022**, *14*, 2237. <https://doi.org/10.3390/sym14112237>

Academic Editors: Xin Wu and Wenbiao Han

Received: 2 October 2022

Accepted: 20 October 2022

Published: 25 October 2022

Publisher's Note: MDPI stays neutral with regard to jurisdictional claims in published maps and institutional affiliations.



Copyright: © 2022 by the authors. Licensee MDPI, Basel, Switzerland. This article is an open access article distributed under the terms and conditions of the Creative Commons Attribution (CC BY) license (<https://creativecommons.org/licenses/by/4.0/>).

Keywords: black hole with scalar hair; rotating black hole; shadow cast

1. Introduction

Recent observations of images from supermassive black holes M87* [1–3] and SgrA* [4,5] by the Event Horizon Telescope (EHT) are significant events in black hole physics, which ushers in a new era for probing the strong gravity regime. The shadow region surrounded by a bright ring is one of important features in the image, which is attributed to the strong gravitational lensing by the black holes. Specifically, there exists a photon region around the black hole, where the light rays from the source are captured such that they cannot form images visible to an outside observer. Then, the unstable photon regions outside the event horizon make it possible to observe the black hole directly. The photons escaping from the spherical orbits form the boundary of the dark silhouette of the black hole, which is known as black hole shadow from the outside observers [6,7]. Thus, the ability of the black hole shadow to indicate the geometry around black hole is widely researched, especially, the characterization of the properties near the horizon [8–27].

The observations from EHT are in good agreement with the predictions of Kerr spacetime in general relativity (GR), which further demonstrates the success of GR. It is well understood that GR needs to be modified or generalized since GR faces challenges in explaining the universe expansion and quantum gravity. Therefore, plenty of modified theories of gravity have been constructed and extensively studied. Nevertheless, EHT observations cannot exclude other black holes in GR or some exotic black holes in modified theories of gravity. In particular, the black hole shadow was used as a new tool to test the no-hair theorem. As one of the simplest manifestation of new physics, the circumvention of the black hole no-hair theorem by producing primary or secondary additional black hole

hair has lately received a lot of interest. In short, the emergence of new fundamental fields in GR, such as the Yang–Mills field [28–31], Skyrme field [32,33], and conformally-coupled scalar field [34], may result in hairy black hole solutions. However, without the existence of matter, hairy black holes may be created by directly coupling the scalar field with the second order algebraic curvature, as in a dilatonic black hole [35–38]. Choosing specific forms of the scalar coupling function activates the onset of spontaneous scalarization and generates the secondary scalar hair of black holes; the coupling terms include Ricci scalar [39,40], Gauss–Bonnet curvature [41,42], Chern–Simons invariant [43], and even matter sources such as Maxwell invariant [44]. Due to the wide extension in this scenario, the shadow of black holes with scalar hair has attracted plenty of attention and remarkable progress has been made [45–54].

More recently, the spherically charged Q-hair solution was constructed in Einstein–Maxwell-scalar gravity with the minimal coupling of the charged scalar field with self-interactions to the gravity [55,56], putting forward the study of formation of hairy black hole. The static charged black hole with scalar Q-hair in this sector are not zero modes of the superradiant instability; instead, the $U(1)$ gauge interaction is primarily responsible for the repulsive force, which is balanced by the gravitational attractive force. Subsequently, many related extensions on this model were explored in the literatures, for instances, hairy solutions and (in)stability analysis with alternative scalar potential formalism [57,58], the inside of the black hole with hair and the holographic superconductor’s likeness [59], black holes with scalar Q-hair in Einstein–Born–Infeld gravity [60] and the extension to five dimensional case [61].

The aim of this paper is to investigate the shadow cast in the static charged black hole with scalar Q-hair constructed in [55,56] as well as in its rotating counterpart. Starting from the null geodesic, we determine the shadow cast in celestial coordinates. We find that the charged black holes with scalar Q-hair beyond GR always have smaller shadow size than the normal black holes, which suggests that the Q-hair compacts the black hole shadow in both non-rotating and rotating cases. Moreover, we study the shadow observables (shadow size and distortion) in the rotating case. It is found that the shadow cast for larger charge parameters has a larger size but smaller distortion, whilst for larger self-interaction parameters, it has smaller size but larger distortion.

This paper is organized as follows. In Section 2, we first review the constructions of the static charged black hole with scalar Q-hair in Einstein–Maxwell-scalar gravity with a self-interacted scalar field, and then construct its rotating counterpart. In Section 3, we work on the null geodesic, the photon sphere and the celestial coordinates which describe the shadow cast. In Section 4, we analyze the black hole shadow cast for non-rotating and rotating cases, respectively. Section 5 provides our closing remarks.

2. Charged Black Holes with Scalar Q-Hair

In this section, we will first review the process of constructing a spherically charged black hole with scalar Q-hair in Einstein–Maxwell-scalar theory, which was proposed in [55,56]. Then, with the use of the Newman–Janis approach [62–65], we generalize the rotating counterpart from the seed of the spherical black hole with scalar Q-hair.

2.1. Spherically Static Black Hole with Scalar Q-Hair

The action of Einstein–Maxwell-scalar gravity, in which the gauge field and charged scalar field minimally couple to the gravity, is given by

$$S = \int d^4x \sqrt{-g} \left(\frac{R}{16\pi G} - F_{\mu\nu} F^{\mu\nu} - (D_\mu \Psi)^\dagger (D^\mu \Psi) - U(\Psi) \right) \quad (1)$$

where R is the Ricci scalar, $F_{\mu\nu} \equiv \partial_\mu A_\nu - \partial_\nu A_\mu$ with the associated gauge 4-potential A_μ , Ψ is a complex scalar field coupled to the Maxwell field by $D_\mu \Psi = \partial_\mu \Psi - ie A_\mu \Psi$ with e the gauge coupling constant. The scalar potential $U(\Psi)$ is taken to be non-negative in the model which should contain the scalar mass and a self-interaction term. As addressed

in [55,56], the simplest formalism reads $U(\Psi) = m^2\Psi^2 - \tau\Psi^4 + \zeta\Psi^6$ where m is the scalar field mass and τ, ζ are positive parameters controlling the strength of the self-interactions.

By varying the action (1) with respect to the metric $g_{\mu\nu}$, scalar field and electromagnetic field, we obtain the following equations of motion

$$R_{\mu\nu} - \frac{1}{2}g_{\mu\nu}R = 8\pi G [T_{\mu\nu}^M + T_{\mu\nu}^S], \tag{2}$$

$$D_\mu D^\mu \Psi = (m^2 - 2\tau\Psi^2 + 3\zeta\Psi^3)\Psi, \tag{3}$$

$$\nabla_\mu F^{\nu\mu} = ie[\Psi^\dagger(D^\nu\Psi) - (D^\nu\Psi^\dagger)\Psi] \equiv ej^\nu, \tag{4}$$

where the terms of energy-momentum tensor are

$$T_{\mu\nu}^M = F_\mu^\gamma F_{\nu\gamma} - \frac{1}{4}g_{\mu\nu}F_{\rho\sigma}F^{\rho\sigma}, \tag{5}$$

$$T_{\mu\nu}^S = D_\mu\Psi^\dagger D_\nu\Psi + D_\nu\Psi^\dagger D_\mu\Psi - g_{\mu\nu} \times \left[\frac{1}{2}g^{\rho\sigma}(D_\rho\Psi^\dagger D_\sigma\Psi + D_\sigma\Psi^\dagger D_\rho\Psi) + U(\Psi) \right], \tag{6}$$

and j^μ is a 4-current satisfying the conserved condition $\partial_j j^\mu = 0$.

In order to construct the solutions for various fields, we take the ansatz on the metric, the gauge field and scalar field as

$$ds^2 = -f(r)dt^2 + \frac{1}{g(r)}dr^2 + r^2(d\theta^2 + \sin^2\theta d\varphi^2), \quad A_\mu dx^\mu = \phi(r)dt, \quad \Psi = \psi(r)e^{-i\omega t} \tag{7}$$

where $f(r) = \sigma(r)^2g(r)$. Because of a local $U(1)$ gauge symmetry, the model is invariant under the transformation

$$\Psi \rightarrow \Psi e^{-eX(x^\nu)}, \quad A_\mu \rightarrow A_\mu + \partial_\mu X(x^\nu) \tag{8}$$

where $X(x^\nu)$ is any real function and x^ν describes the coordinate parameters. Thus, we can choose the gauge to set $\omega = 0$ without loss of generality in the following discussion.

Subsequently, the corresponding field Equations (2)–(4) with respect to the ansatz are rewritten as

$$g'(r)r = 1 - g(r) - 4\pi G r^2 \left[\frac{\phi'^2(r)}{2\sigma^2(r)} + g(r)\psi'^2 + U(\psi(r)) + \frac{e^2\phi^2}{g(r)\sigma^2(r)}\psi^2(r) \right], \tag{9}$$

$$\sigma'(r) = 8\pi G r \sigma(r) \left[\psi'^2(r) + \frac{e^2\phi^2(r)\psi^2(r)}{g(r)^2\sigma^2(r)} \right], \tag{10}$$

$$\phi''(r) + \left(\frac{2}{r} - \frac{\sigma'(r)}{\sigma(r)} \right) \phi'(r) - \frac{2e^2\phi(r)\psi^2(r)}{g(r)} = 0, \tag{11}$$

$$\psi''(r) + \left(\frac{2}{r} + \frac{g'(r)}{g(r)} + \frac{\sigma'(r)}{\sigma(r)} \right) \psi'(r) + \frac{e^2\phi^2(r)\psi(r)}{g(r)^2\sigma^2(r)} - \frac{1}{g(r)} \left(m^2\psi(r) - 2\tau\psi^3(r) + 3\zeta\psi^5(r) \right) = 0. \tag{12}$$

Moreover, according to the analysis on scaling symmetry in [55], the system has only three independent dimensionless input parameters

$$\alpha_0^2 = \frac{4\pi G m^2}{\tau}, \quad \beta_0^2 = \frac{\zeta m^2}{\tau^2}, \quad q = \frac{e}{\sqrt{\tau}}. \tag{13}$$

To solve the full equations of motion numerically, we have to fix the boundary conditions. On the horizon $r = r_h$, we should have

$$\phi(r_h) = 0, \quad g(r_h) = 0 \tag{14}$$

to guarantee the existence of black hole solutions, while $\phi(r)dt$ is well defined, and other field functions are regular.

Near infinity for $r \rightarrow \infty$, the functions for the fields behave as

$$g(r) \rightarrow 1 - \frac{2M}{r} - \frac{\alpha_0^2 Q_e^2}{r^2} + \dots, \quad (15)$$

$$\sigma(r) \rightarrow 1, \quad (16)$$

$$\phi(r) \rightarrow \phi_0 - \frac{Q_e}{r} + \dots, \quad (17)$$

$$\psi(r) \rightarrow \frac{\psi_0}{r} e^{-m_\infty r} + \dots, \quad (18)$$

where $m_\infty \equiv \sqrt{m^2 - e^2 \phi_0^2}$ implying $m \geq e \phi_0$. Here, M is the ADM mass of the black hole, ϕ_0 is the chemical potential, and $Q_e = Q_{BH} + e Q_N$ is the total electric charge. $Q_N = \frac{1}{4\pi} \int d^3x \sqrt{-g} j^t$ is the conserved No-ether charges in the radial direction and Q_{BH} is the electric charge of black hole $Q_{BH} = \frac{1}{4\pi} \oint_H dS_r F^{tr}$.

With the boundary conditions stated above, the group of equations of motion (9)–(12) is solved. To this end, we employ the spectral method. The basic idea of the spectral method is to expand differential equations under a finite number of bases polynomials to obtain the matrix of the differential equations. Thus, solving the differential equations is replaced by calculating the eigenvalues of the matrices. More details on spectral method and its applications in general relativity can be found in [66–73] and therein. In the equation, we set $m = \tau = 1$ for convenience. Depending on the choices of the input parameters, we can produce the charged black hole without or with the Q-scalar hair, and the signal of the black hole with scalar Q-hair is the existence of a non-zero solution of $\psi(r)$. We show a sample of charged black holes with scalar Q-hair in Figure 1, where we plot the metric functions $g(r)$, $\sigma(r)$, the electric field $\phi(r)$, and the scalar field $\psi(r)$ for the parameters $\alpha_0 = 0.068$, $\beta_0 = \sqrt{0.6}$, and $q = 0.08$. More solutions with scalar Q-hair in the sector will be produced in later studies.

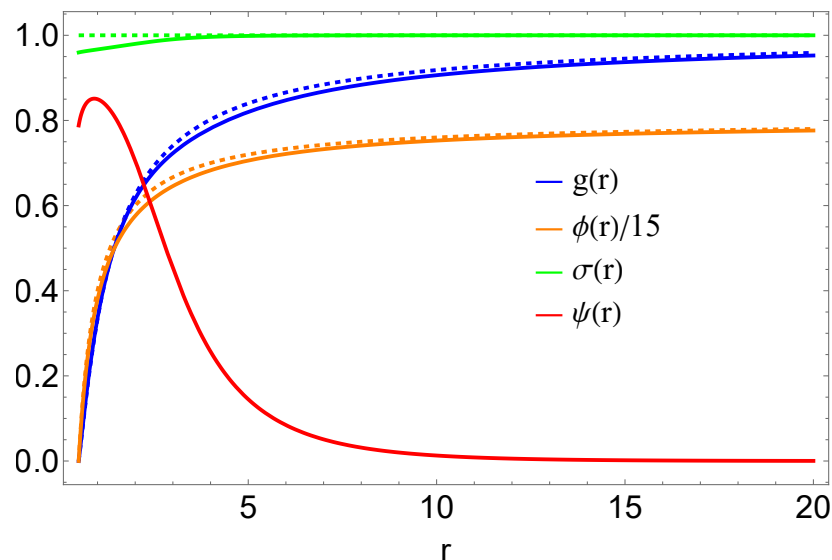


Figure 1. The metric functions $g(r)$, $\sigma(r)$, the electric field $\phi(r)$, and the scalar field $\psi(r)$ for $\alpha_0 = 0.068$, $\beta_0 = \sqrt{0.6}$ and $q = 0.08$. The dashed curves are the corresponding functions of no-hair black hole, i.e., the RN black hole.

2.2. Rotating Charged Black Hole with Scalar Q-Hair

Since non-rotating black hole tests are rare, as the spinning of black holes is crucial in many astrophysical processes, rotating black hole solutions could provide an arena to test the theories of gravity via astrophysical observation. Thus, in this subsection, we shall use the Newman–Janis approach to generate a stationary and axisymmetric metric from the seed of spherically static solutions with scalar Q-hair. As mentioned in [62–65], the original

formalism is constrained by the non-trivial requirement that the final transformation to Boyer–Lindquist coordinates necessitates *theta*-independent functions, resulting in the difficulty that it cannot be extended to a generic spherically symmetric metric. To bypass the limitation, the authors of [65] considered the slowly-rotating limit. Here, we employ the improved formalism in [62,64] by introducing an arbitrary undetermined function.

To proceed, we introduce $du = dt - \frac{dr}{\sqrt{f(r)g(r)}}$ and transform the metric (7) into the Eddington–Finkelstein coordinates

$$ds^2 = -f(r)du^2 - 2\sqrt{\frac{f}{g}}dudr + r^2(d\theta^2 + \sin^2\theta d\varphi^2). \tag{19}$$

The inverse metric $g^{\mu\nu}$ can be expressed by a null tetrad $(l^\mu, n^\mu, m^\mu, m^{\dagger\mu})$ as

$$g^{\mu\nu} = -l^\mu n^\nu - l^\nu n^\mu + m^\mu m^{\dagger\nu} + m^\nu m^{\dagger\mu}. \tag{20}$$

The tetrad vectors should satisfy [62]

$$l_\mu l^\mu = n_\mu n^\mu = m_\mu m^\mu = l_\mu m^\mu = n_\mu m^\mu = 0, \tag{21}$$

$$l_\mu n^\mu = -m_\mu m^{\dagger\mu} = -1, \tag{22}$$

which in our case could be the formalism

$$l^\mu = \delta_r^\mu, \quad n^\mu = \sqrt{\frac{g(r)}{f(r)}}\delta_u^\mu - \frac{g(r)}{2}\delta_r^\mu, \quad m^\mu = \frac{1}{\sqrt{2r^2}}\left(\delta_\theta^\mu + \frac{i}{\sin\theta}\delta_\varphi^\mu\right) \tag{23}$$

with δ_ν^μ the Kronecker Delta.

Subsequently, with complex coordinate transformations $u' = u - ia \cos\theta$ and $r' = r + ia \cos\theta$, the tetrad is then rewritten as

$$l'^\mu = \delta_r^\mu, \quad n'^\mu = \sqrt{\frac{g(r')}{f(r')}}\delta_u^\mu - \frac{g(r')}{2}\delta_r^\mu, \tag{24}$$

$$m'^\mu = \frac{1}{\sqrt{2(r'-ia \cos\theta)^2}}\left(ia \sin\theta(\delta_u^\mu - \delta_r^\mu) + \delta_\theta^\mu + \frac{i}{\sin\theta}\delta_\varphi^\mu\right) \tag{25}$$

where a is introduced as the spin parameter of the axisymmetric black hole. Then, the new inverse metric is constructed by $g'^{\mu\nu} = -l'^\mu n'^\nu - l'^\nu n'^\mu + m'^\mu m'^{\dagger\nu} + m'^\nu m'^{\dagger\mu}$, whose explicit formula is

$$ds^2 = -f(r')du^2 - 2\sqrt{\frac{f(r')}{g(r')}}dudr' + 2a \sin^2\theta\left(f(r') - \sqrt{\frac{f(r')}{g(r')}}\right)dud\varphi + 2a\sqrt{\frac{f(r')}{g(r')}}\sin^2\theta drd\varphi + (r' - ia \cos\theta)^2 d\theta^2 + \sin^2\theta\left[(r' - ia \cos\theta)^2 + a^2 \sin^2\theta\left(2\sqrt{\frac{f(r')}{g(r')}} - f(r')\right)\right]d\varphi^2. \tag{26}$$

The final step is to transform the new metric into the Boyer-Lindquist coordinates with the transformations

$$du = dt' + \lambda(r)dr, \quad d\varphi = d\varphi' + \chi(r)dr \tag{27}$$

where the transformation functions are

$$\lambda(r) = -\frac{k(r) + a^2}{g(r)r^2 + a^2}, \quad \chi(r) = -\frac{a}{g(r)r^2 + a^2}, \quad k(r) = \sqrt{\frac{g(r)}{f(r)}}r^2. \tag{28}$$

Thus, the new metric under the Boyer-Lindquist coordinates is

$$\begin{aligned}
 ds^2 &= -F(r, \theta)dt^2 - 2a \sin^2 \theta \left(\sqrt{\frac{F(r, \theta)}{G(r, \theta)}} - F(r, \theta) \right) dt d\varphi + \frac{H(r, \theta)}{\Delta(r)} dr^2 + \\
 &H(r, \theta)d\theta^2 + \sin^2 \theta \left[H(r, \theta) + a^2 \sin^2 \theta \left(2\sqrt{\frac{F(r, \theta)}{G(r, \theta)}} - F(r, \theta) \right) \right] d\varphi^2 \quad (29)
 \end{aligned}$$

with the metric functions

$$F(r, \theta) = \frac{g(r)r^2 + a^2 \cos^2 \theta}{(k(r) + a^2 \cos^2 \theta)^2} H(r, \theta), \quad G(r, \theta) = \frac{g(r)r^2 + a^2 \cos^2 \theta}{H(r, \theta)}. \quad (30)$$

In the above metric, $\Delta(r) = G(r, \theta)H(r, \theta) + a^2 \sin^2 \theta = g(r)r^2 + a^2$ and $H(r, \theta)$ is the arbitrary undetermined function. As proposed in [64], imposing the additional condition $G_{r\theta} = 0$ could fix $H(r, \theta)$ as $H(r, \theta) = r^2 + a^2 \cos^2 \theta$.

The metrics (29) and (30) provide the stationary and axisymmetric counterpart of the spherically symmetric solution (7) by inserting the corresponding $f(r)$ and $g(r)$. It will reduce to the static case as the spin parameter a vanishes. If the inserted $f(r)$ and $g(r)$ are solutions with the scalar Q-hair, then (29) and (30) describe the rotating black hole with scalar Q-hair; otherwise, they correspond to the Kerr–Newmann black hole. Due to the numerical origin, it is difficult to determine the interior geometry of the solution; however, we present the samples of $\Delta(r)$ and g_{tt} for the exterior geometry in Figure 2, where the radii with $\Delta(r) = 0$ and $g_{tt} = 0$ determine the location of the outer horizon and static limit surface, respectively.

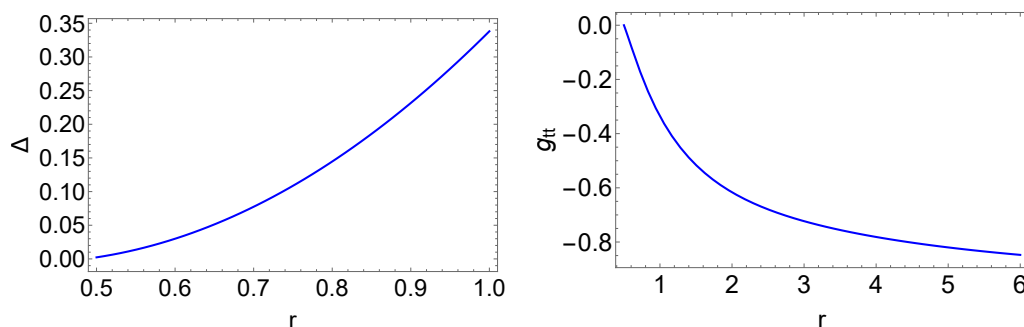


Figure 2. The samples of $\Delta(r)$ and g_{tt} for the exterior geometry, where we have fix $\alpha_0 = 0.068$, $\beta_0 = \sqrt{0.6}$, $q = 0.008$ and $a/M = 0.1$.

3. Null Geodesic and Celestial Coordinates

In this section, we will investigate the null geodesics and focus on the photons with circular orbits in the background of (29). The geodesics of photon orbiting in spacetime can be obtained using the Hamilton–Jacobi approach [74], and the associated equation is

$$\frac{\partial \mathcal{S}}{\partial \lambda} + \frac{1}{2} g^{\mu\nu} \frac{\partial \mathcal{S}}{\partial x^\mu} \frac{\partial \mathcal{S}}{\partial x^\nu} = 0 \quad (31)$$

where \mathcal{S} is the Jacobi action of the photon, λ is the affine parameter of the null geodesic and the momentum p_μ is defined by

$$p_\mu = \frac{\partial \mathcal{S}}{\partial x^\mu} = g_{\mu\nu} \frac{dx^\nu}{d\lambda}. \quad (32)$$

The spacetime has two Killing vectors ∂_t and ∂_φ , which suggest two motion constants, i.e., the orbital energy E and orbital angular momentum L_φ , respectively

$$E = -g_{t\mu} \frac{\partial x^\mu}{\partial \lambda}, \quad (33)$$

$$L_\varphi = g_{\varphi\mu} \frac{\partial x^\mu}{\partial \lambda}. \quad (34)$$

So, the Jacobi action can be separated as follows:

$$S = -Et + L_\varphi \varphi + \mathcal{S}_r(r) + \mathcal{S}_\theta(\theta) \quad (35)$$

where the functions $\mathcal{S}_r(r)$ and $\mathcal{S}_\theta(\theta)$ depend only on r and θ , respectively. Substituting the Jacobi action (35) into the Hamilton-Jacobi Equation (31), we can obtain

$$\left(\frac{d\mathcal{S}_r}{dr} \right) = \sqrt{\frac{R(r)}{\Delta(r)}}, \quad (36)$$

$$\left(\frac{d\mathcal{S}_\theta}{d\theta} \right) = \sqrt{\Theta(\theta)}, \quad (37)$$

with

$$R(r) = [\Sigma(r)E - aL_\varphi]^2 - \Delta(r) [\mathcal{K} + (L_\varphi - aE)^2] \quad (38)$$

$$\Theta(\theta) = \mathcal{K} + a^2 E^2 \cos^2 \theta - L_\varphi^2 \cot^2 \theta \quad (39)$$

where $\Sigma(r) = \sqrt{\frac{G}{F}} H + a^2 \sin^2 \theta = k(r) + a^2$ and \mathcal{K} is the Carter constant of the motion related to the Killing–Yano tensor [74] due to the integrability of the system. Furthermore, by combining the null geodesic condition $p^\mu p_\mu = 0$ with the results (36) and (37), we can obtain four equations of motion which control the photon orbits.

$$\begin{aligned} \frac{F(r, \theta)}{G(r, \theta)} \Delta(r) \frac{dt}{d\lambda} &= \left[H(r, \theta) + a^2 \sin^2 \theta \left(2\sqrt{\frac{F(r, \theta)}{G(r, \theta)}} - F(r, \theta) \right) \right] E \\ &\quad - aL_\varphi \left(\sqrt{\frac{F(r, \theta)}{G(r, \theta)}} - F(r, \theta) \right), \end{aligned} \quad (40)$$

$$\frac{F(r, \theta)}{G(r, \theta)} \Delta(r) \sin^2 \theta \frac{d\varphi}{d\lambda} = a \sin^2 \theta \left(\sqrt{\frac{F(r, \theta)}{G(r, \theta)}} - F \right) E + F(r, \theta) L_\varphi, \quad (41)$$

$$H(r, \theta) \frac{dr}{d\lambda} = \pm \sqrt{R(r)}, \quad (42)$$

$$H(r, \theta) \frac{d\theta}{d\lambda} = \pm \sqrt{\Theta(\theta)}. \quad (43)$$

To solve the above system of equations, symplectic algorithms are usually used in celestial mechanics, such as the explicit symplectic algorithms in general relativity [75–78], explicit symmetric algorithms for an inseparable system [79,80], as well as explicit and implicit mixed symplectic algorithms [81,82]. Here, we are interested in the shadow cast of the black hole; so, only the photons with unstable circular orbits are relevant. Therefore, we focus on the radial equation of motion (42), which is rewritten as

$$\left(H(r, \theta) \frac{dr}{d\lambda} \right)^2 + V_{orb}(r) = 0, \quad (44)$$

with the effective potential

$$\frac{V_{orb}(r)}{E^2} = -[\Sigma(r) - a\zeta]^2 + \Delta(r) [\eta + (\zeta - a)^2]. \tag{45}$$

In the formula, we have defined $\zeta \equiv L_\phi/E$ and $\eta \equiv \mathcal{K}/E^2$ which are known as impact parameters determining the shape of the black hole shadow, as we will see soon. The unstable circular photon orbits with radius $r = r_p$ should satisfy the following conditions

$$V_{orb}(r_p) = 0, \quad \frac{\partial V_{orb}(r_p)}{\partial r} = 0, \quad \frac{\partial^2 V_{orb}(r_p)}{\partial r^2} < 0, \tag{46}$$

from which we can solve out the impact parameters in terms of the metric functions as

$$\zeta(r_p) = \frac{\Sigma(r)\Delta'(r) - 2\Delta(r)\Sigma'(r)}{a\Delta'(r)} \Big|_{r=r_p}, \tag{47}$$

$$\eta(r_p) = \frac{4a^2\Sigma(r)^2\Delta(r) - [(\Sigma(r) - a^2)\Delta(r)' - 2\Sigma(r)'\Delta(r)]^2}{a^2\Delta(r)^2} \Big|_{r=r_p}. \tag{48}$$

Then, by inserting the above formulas into (43), the condition $\Theta(\theta) \geq 0$ provides an inequality which in fact determines the photon region of the black hole. This means that for each point in the region, there exists a light-like geodesic staying in the circular orbit $r = r_p$, along which φ is governed by the equation of motion (41) and θ can oscillate between the extrema determined by $\Theta(\theta) = 0$.

With the impact parameters in hand, we are ready to determine the shadow boundary of the rotating black holes. To this end, we construct the celestial coordinates (α, β) to fix the shape of shadow. As shown in Figure 3, the coordinate α denotes the apparent perpendicular distance of the image as seen from the axis, and the coordinate β denotes the apparent perpendicular distance of the image from its projection on the equatorial plane. For the observations at spatial infinity with the Boyer–Lindquist coordinate (r_0, θ_0) , the shadow boundary in the celestial coordinate can be described by [83–85]

$$\alpha = \lim_{r_0 \rightarrow \infty} \left(-r_0^2 \sin \theta_0 \frac{d\varphi}{dr} \Big|_{(r=r_0, \theta=\theta_0)} \right), \tag{49}$$

$$\beta = \pm \lim_{r_0 \rightarrow \infty} \left(r_0^2 \frac{d\theta}{dr} \Big|_{(r=r_0, \theta=\theta_0)} \right), \tag{50}$$

where r_0 also denotes the distance from the very far observer to the black hole and θ_0 is the inclination between the observer’s line of sight and the black hole’s spin axis. Calculating $\frac{d\varphi}{dr}$ and $\frac{d\theta}{dr}$ from the geodesic equations and considering the conditions for the unstable circular orbits, we can simplify the celestial coordinate as follows:

$$\alpha(r_p) = -\frac{\zeta(r_p)}{\sin \theta_0}, \tag{51}$$

$$\beta(r_p) = \pm \sqrt{\eta(r_p) + a^2 \cos^2 \theta_0 - \zeta(r_p)^2 \cot^2 \theta_0}. \tag{52}$$

Next, we shall apply the numerical results of the static charged solution with scalar hair and its rotating generalization into the celestial coordinates (α, β) , and analyze the shadow cast affected by the scalar hair.

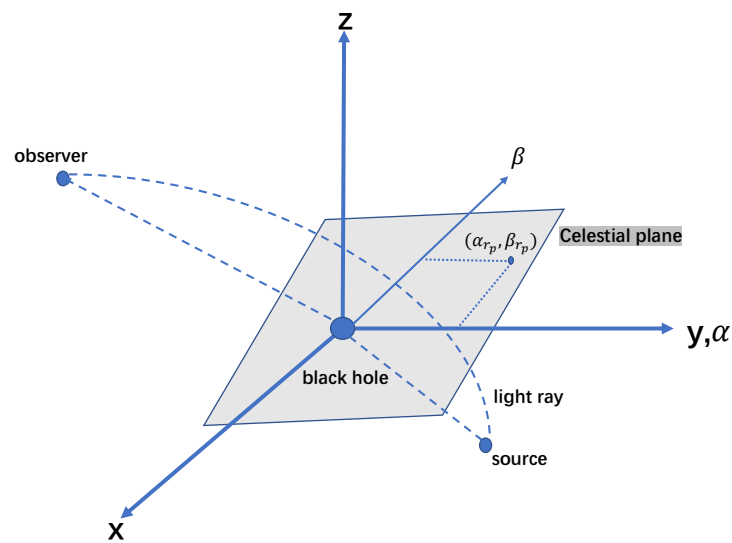


Figure 3. Cartoon of the very far distant observer’s celestial plane (the shaded region), and the celestial coordinates $(\alpha_{r_p}, \beta_{r_p})$ which can be evaluated by Equations (49) and (50).

4. Black Hole Shadow Cast

4.1. Shadow Cast for Non-Rotating Black Hole with Scalar Q-Hair

We first explore the black hole shadow cast for spherically symmetric spacetime, i.e., $a = 0$ described by the metric (7). By tuning the model parameters, we numerically work out the corresponding metric functions $\sigma(r)$ and $g(r)$ for the black holes with scalar Q-hair, and their prior shift from the RN black hole should be reflected in the black hole shadow casts.

In this case, we can follow the steps in the review [7] for the spherical static black hole to derive the radius of the photo sphere and shadow boundary. Therefore, the radius of the photo sphere, r_s , satisfies

$$f'(r_s)r_s - 2f(r_s) = 0 \quad (53)$$

and the radius of shadow cast is given by

$$R_s = \sqrt{\frac{r_s^2}{f(r_s)}}, \quad (54)$$

showing that the shadow cast is a perfect circle.

We show the shadow casts for black holes with scalar Q-hair in Einstein–Maxwell–scalar gravity for various parameters (α_0, β_0, q) in Figure 4. The parameters (α_0, β_0, q) could correspond to different configurations of various fields for the solutions, which then have a different shadow cast as shown in the figure. In detail, increasing the coupling q enlarges the shadow size of the black hole with scalar Q-hair, but increasing the parameters α_0 or β_0 makes the shadow size smaller. Moreover, it is obvious that q has a more profound impact than α_0 and β_0 , which is reasonable because α_0 or β_0 indicates higher order coupling between the fields. In addition, the shadow cast of a black hole with scalar Q-hair is always smaller than that of a black hole RN black hole, which is denoted by the dashed circle in each plot. Since the charge in the RN black hole could decrease the shadow size [86], we can further conclude that the shadow size of a non-rotating black hole with scalar Q-hair is smaller than that of the Schwarzschild black hole.

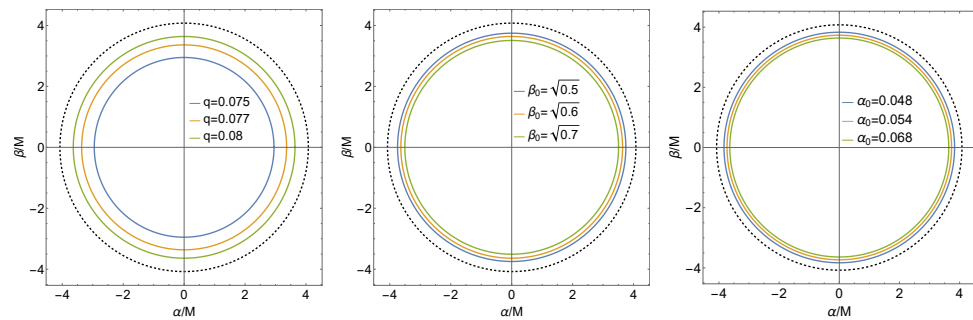


Figure 4. The shadows of non-rotating case for different q , α_0 and β_0 . In the left plot, we fix $\alpha_0 = 0.068$ and $\beta_0 = \sqrt{0.6}$. In the middle plot, we fix $q = 0.008$ and $\beta_0 = \sqrt{0.6}$. In the right plot, $\alpha_0 = 0.068$ and $q = 0.008$ are fixed. The black dashed cycle in each plot represents the shadow of black hole without scalar hair which is RN black hole.

4.2. Shadow for the Rotating Black Hole with Scalar Q-Hair

Now, we turn on the spin parameter and figure out the shadow casts for the rotating black holes with scalar Q-hair which we constructed in Section 2.2. It should be noted that in our case, the rotating solutions are only available for small spin parameter a and large a will destroy their stability, because the numeric can only provide the static profiles outside the black hole horizon. The results are shown in Figures 5 and 6. It is shown in Figure 5 that the shadow becomes more distorted as a increases, which is the same as that in Kerr and KN black holes. As shown in Figure 6 with $a/M = 0.1$, the shadow size diminishes for larger α_0 or β_0 ; yet, it is enhanced by the coupling parameter q . In addition, the size of a rotating charged black hole with scalar Q-hair is always smaller than that of a KN black hole denoted by the dashed curves. Moreover, since the shadow size of KN black hole is smaller than that of a Kerr black hole [7,8], the size of a rotating charged black hole with scalar Q-hair will also be smaller than that of a Kerr black hole. These influences of the model parameters on the shadow size are similar to that in the static case.

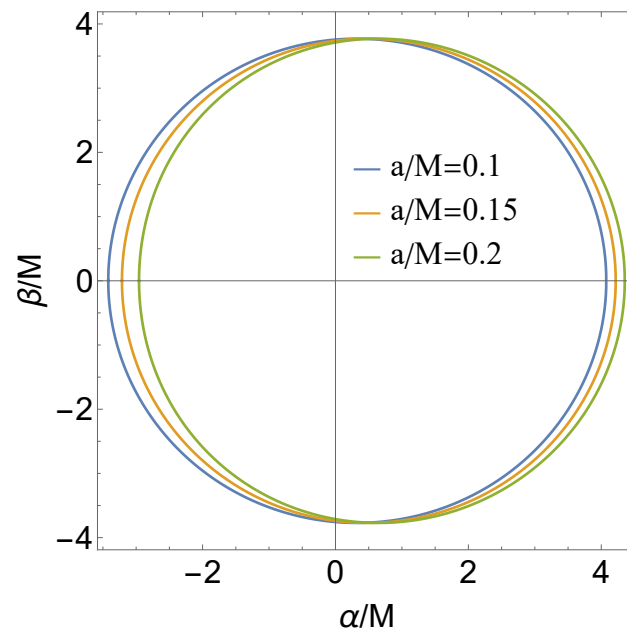


Figure 5. The shadows cast of rotating charged black hole with scalar hair for different a , where we have a fixed $\alpha_0 = 0.068$, $\beta_0 = \sqrt{0.6}$ and $q = 0.008$.

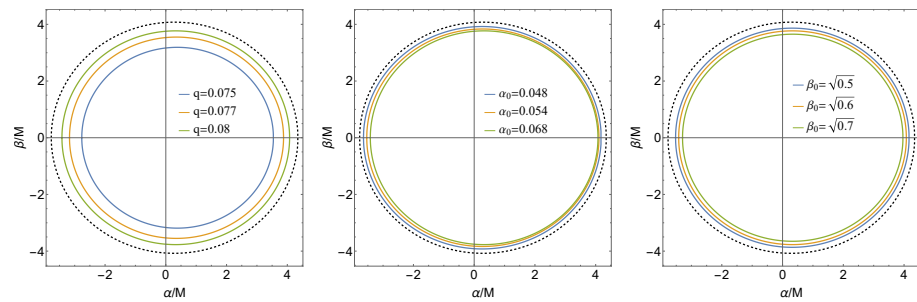


Figure 6. The shadows cast of rotating charged black hole with scalar hair for $a/M = 0.1$ with different q (fixing $\alpha_0 = 0.068$, $\beta_0 = \sqrt{0.6}$), α_0 (fixing $q = 0.008$, $\beta_0 = \sqrt{0.6}$) and β_0 (fixing $\alpha_0 = 0.068$, $q = 0.008$), respectively. The black dashed curve in each plot is the shadow cast of Kerr-Newmann black hole.

Then, to carefully study the effect of parameters on the shadow cast, it is important to connect them with astronomical observables which could be easily measured and are helpful to test black hole parameters. Here, we consider the following two characterized observables: R_s , the radius of the reference circle for the distorted shadow, and δ_s , the deviation of the left edge of the shadow from the reference circle boundary. To define the black hole observables, we indicate the top, bottom, right and left of the shadow cast as (X_t, Y_t) , (X_b, Y_b) , $(X_r, 0)$ and $(X_l, 0)$, respectively, and $(X'_l, 0)$ as the leftmost edge of the reference circle. Thus, the characterized observables are defined via [87]

$$R_s = \frac{(X_t - X_r)^2 + Y_t^2}{2 |X_r - X_t|}, \quad \delta_s = \frac{|X_l - X'_l|}{R_s}. \tag{55}$$

For the shadow of the non-rotating case, we have $\delta_s = 0$ because the shadow is a perfect circle such that $X_l = X'_l$. The results of R_s and δ_s related with each plot in Figure 6 are listed in Tables 1–3. With the increase in q , the shadow size increases while the distortion becomes smaller, but when the parameter α_0 or β_0 increases, the shadow size decreases while the distortion becomes larger. The results indicate that q has a competitive relation with α_0 or β_0 in the influence of shadow observables. We discuss the possible interpretation of these results in the conclusion section.

Table 1. The shadow radius R_s and the distortion δ_s for samples of q with $\alpha_0 = 0.068$ and $\beta_0 = \sqrt{0.6}$.

q	0.08	0.077	0.075
R_s	3.7703	3.5507	3.1894
δ_s	0.0116	0.01490	0.0213

Table 2. The shadow radius R_s and the distortion δ_s for samples of α_0 for $q = 0.008$ and $\beta_0 = \sqrt{0.6}$.

α_0	0.068	0.054	0.048
R_s	3.7703	3.8356	3.9230
δ_s	0.0116	0.0062	0.0039

Table 3. The shadow radius R_s and the distortion δ_s for samples of β_0 with $q = 0.008$ and $\alpha_0 = 0.068$.

β_0	$\sqrt{0.7}$	$\sqrt{0.6}$	$\sqrt{0.5}$
R_s	3.6526	3.7703	3.8657
δ_s	0.0127	0.0116	0.0106

5. Closing Remarks

In the Einstein–Maxwell–scalar theory with the self-interacted scalar field minimally coupled with a Maxwell field and gravity field, the spherical statically charged black hole

with scalar Q-hair was constructed via circumvention of the black hole no-hair theorem in [55,56]. In this paper, starting from the null geodesic, we studied the optical feature of these black holes with scalar Q-hair as well as their rotating counterpart which we constructed with the use of the Newman–Janis approach.

We mainly focused on the shadow cast of the non-rotating and rotating black holes with scalar Q-hairs. Compared to RN and KN black holes, the charged black holes with scalar Q-hair in the current model always have a smaller shadow size. This feature is similar to the finding for the Kerr black hole with scalar hair in [47,48]. The possible interpretation could be as follows. The presence of the scalar field provides the repulsive force which could balance the black hole's attraction, such that the cohesive scalar hairs can be formed surrounding the black hole. Nevertheless, the presence of scalar hairs seems to lead the center black hole to shrink because they carry a part of the total energy of the entire sector.

Moreover, we found that the model parameters have a significant affect on shadow observables. Increasing the charge parameter q would increase the shadow size but decrease the shadow distortion in an axisymmetric black hole with scalar Q-hair, whereas increased interacting parameters α_0 as well as β_0 would decrease their shadow size but increase the shadow distortion. This implies that the larger q results in stronger repulsive forces as coulombic force is stronger, but a larger α_0 or β_0 leads to weaker repulsive forces to compete with gravity. In-depth studies about the effect of model parameters on shadow distortion should be undertaken.

One interesting direction is to test the nature of supermassive black holes in M87* and SgrA* modeled with the black hole with scalar hair in the current model. This will be beneficial in terms of the following two aspects: (i) With the help of EHT observation, it may provide a possible way to diagnose gravity with scalar field from GR by the black hole shadow. (ii) Compared with the EHT observation, the black hole shadow could shed light on the test of the no-hair theorem of black holes.

Author Contributions: The authors contributed equally in the preparation of this article. All authors have read and agreed to the published version of the manuscript.

Funding: This research was funded by Natural Science Foundation of Jiangsu Province under Grant No.BK20211601 and Fok Ying Tung Education Foundation under Grant No. 171006.

Data Availability Statement: Not applicable.

Conflicts of Interest: The authors declare no conflict of interest.

References

1. The Event Horizon Telescope Collaboration; Akiyama, K.; Alberdi, A.; Alef, W.; Asada, K.; Azuly, R. First M87 Event Horizon Telescope Results. I. The Shadow of the Supermassive Black Hole. *Astrophys. J. Lett.* **2019**, *875*, L1. [[CrossRef](#)]
2. The Event Horizon Telescope Collaboration; Akiyama, K.; Alberdi, A.; Alef, W.; Asada, K.; Azuly, R.; Baczkó, A.-K.; Ball, D.; Baloković, M.; Barrett, J.; et al. First M87 Event Horizon Telescope Results. VI. The Shadow and Mass of the Central Black Hole. *Astrophys. J. Lett.* **2019**, *875*, L6. [[CrossRef](#)]
3. The Event Horizon Telescope Collaboration; Akiyama, K.; Alberdi, A.; Alef, W.; Asada, K.; Azuly, R.; Baczkó, A.-K.; Ball, D.; Baloković, M.; Barret, J.; et al. First M87 Event Horizon Telescope Results. IV. Imaging the Central Supermassive Black Hole. *Astrophys. J. Lett.* **2019**, *875*, L4. [[CrossRef](#)]
4. The Event Horizon Telescope Collaboration; Akiyama, K.; Alberdi, A.; Alef, W.; Algaba, J.C.; Anantua, R.; Asada, K.; Azuly, R.; Bach, U.; Baczkó, A.-K.; et al. First Sagittarius A* Event Horizon Telescope Results. I. The Shadow of the Supermassive Black Hole in the Center of the Milky Way. *Astrophys. J. Lett.* **2022**, *930*, L12. [[CrossRef](#)]
5. The Event Horizon Telescope Collaboration; Akiyama, K.; Alberdi, A.; Alef, W.; Algaba, J.C.; Anantua, R.; Asada, K.; Azuly, R.; Bach, U.; Baczkó, A.-K.; et al. First Sagittarius A* Event Horizon Telescope Results. VI. Testing the Black Hole Metric. *Astrophys. J. Lett.* **2022**, *930*, L17. [[CrossRef](#)]
6. Cunha, P.V.P.; Herdeiro, C.A.R. Shadows and strong gravitational lensing: A brief review. *Gen. Relativ. Gravit.* **2018**, *50*, 42. [[CrossRef](#)]
7. Perlick, V.; Tsupko, O.Y. Calculating black hole shadows: Review of analytical studies. *Phys. Rep.* **2022**, *947*, 1–39. [[CrossRef](#)]
8. Grenzbach, A.; Perlick, V.; Lämmerzahl, C. Photon Regions and Shadows of Kerr–Newman–NUT Black Holes with a Cosmological Constant. *Phys. Rev. D* **2014**, *89*, 124004. [[CrossRef](#)]

9. Cunha, P.V.P.; Herdeiro, C.A.R.; Radu, E. EHT constraint on the ultralight scalar hair of the M87 supermassive black hole. *Universe* **2019**, *5*, 220. [[CrossRef](#)]
10. Bambi, C.; Freese, K.; Vagnozzi, S.; Visinelli, L. Testing the rotational nature of the supermassive object M87* from the circularity and size of its first image. *Phys. Rev. D* **2019**, *100*, 044057. [[CrossRef](#)]
11. Wang, H.-M.; Xu, Y.-M.; Wei, S.-W. Shadows of Kerr-like black holes in a modified gravity theory. *J. Cosmol. Astropart. Phys.* **2019**, *2019*, 46. [[CrossRef](#)]
12. Guo, M.; Obers, N.A.; Yan, H. Observational signatures of near-extremal Kerr-like black holes in a modified gravity theory at the Event Horizon Telescope. *Phys. Rev. D* **2018**, *98*, 084063. [[CrossRef](#)]
13. Kumar, R.; Ghosh, S.G.; Wang, A. Shadow cast and deflection of light by charged rotating regular black holes. *Phys. Rev. D* **2019**, *100*, 124024. [[CrossRef](#)]
14. Ghosh, S.G.; Kumar, R.; Islam, S.U. Parameters estimation and strong gravitational lensing of nonsingular Kerr-Sen black holes. *J. Cosmol. Astropart. Phys.* **2021**, *3*, 56. [[CrossRef](#)]
15. Jha, S.K.; Rahaman, A. Lorentz violation and noncommutative effect on superradiance scattering off Kerr-like black hole and on the shadow of it. *arXiv* **2022**, arXiv:2111.02817.
16. Khodadi, M.; Lambiase, G.; Mota, D.F. No-hair theorem in the wake of Event Horizon Telescope. *J. Cosmol. Astropart. Phys.* **2021**, *9*, 28. [[CrossRef](#)]
17. Meng, Y.; Kuang, X.-M.; Tang, Z.-Y. Photon regions, shadow observables, and constraints from M87* of a charged rotating black hole. *Phys. Rev. D* **2022**, *106*, 064006. [[CrossRef](#)]
18. Kuang, X.-M.; Tang, Z.-Y.; Wang, B.; Wang, A. Constraining a modified gravity theory in strong gravitational lensing and black hole shadow observations. *Phys. Rev. D* **2022**, *106*, 064012. [[CrossRef](#)]
19. Kuang, X.-M.; Övgün, A. Strong gravitational lensing and shadow constraint from M87* of slowly rotating Kerr-like black hole. *Ann. Phys.* **2022**, *169147*. in press. [[CrossRef](#)]
20. Tang, Z.-Y.; Kuang, X.-M.; Wang, B.; Qian, W.-L. The length of a compact extra dimension from shadow. *arXiv* **2022**, arXiv:2206.08608.
21. Vagnozzi, S.; Roy, R.; Tsai, Y.D.; Visinelli, L. Horizon-scale tests of gravity theories and fundamental physics from the Event Horizon Telescope image of Sagittarius A*. *arXiv* **2022**, arXiv:2205.07787.
22. Chen, C.-Y. Testing black hole equatorial reflection symmetry using Sgr A* shadow images. *Phys. Rev. D* **2022**, *106*, 044009. [[CrossRef](#)]
23. Chen, Y.; Roy, R.; Vagnozzi, S.; Visinelli, L. Superradiant evolution of the shadow and photon ring of Sgr A*. *Phys. Rev. D* **2022**, *106*, 043021. [[CrossRef](#)]
24. Wang, M.; Chen, S.; Jing, J. Chaotic shadows of black holes: A short review. *Commun. Theor. Phys.* **2022**, *74*, 097401.
25. Hu, S.; Deng, C.; Li, D.; Wu, X.; Liang, E. Observational signatures of Schwarzschild-MOG black holes in scalar-tensor-vector gravity: shadows and rings with different accretions. *Eur. Phys. J. C* **2022**, *82*, 885. [[CrossRef](#)]
26. Cao, W.; Liu, W.; Wu, X. Integrability of Kerr-Newman spacetime with cloud strings, quintessence and electromagnetic field. *Phys. Rev. D* **2022**, *105*, 124039. [[CrossRef](#)]
27. Chen, Y.-X.; Mou, P.-H.; Li, G.-P. The observational shadow features of a renormalization group improved black hole considering spherical accretions. *Symmetry* **2022**, *14*, 1959. [[CrossRef](#)]
28. Volkov, M.S.; Galtsov, D.V. NonAbelian Einstein Yang-Mills black holes. *JETP Lett.* **1989**, *50*, 346–350.
29. Bizon, P. Colored black holes. *Phys. Rev. Lett.* **1990**, *64*, 2844–2847. [[CrossRef](#)]
30. Greene, B.R.; Mathur, S.D.; O’Neill, C.M. Eluding the no hair conjecture: Black holes in spontaneously broken gauge theories. *Phys. Rev. D* **1993**, *47*, 2242–2259. [[CrossRef](#)]
31. Maeda, K.-I.; Tachizawa, T.; Torii, T.; Maki, T. Stability of nonAbelian black holes and catastrophe theory. *Phys. Rev. Lett.* **1994**, *72*, 450–453. [[CrossRef](#)]
32. Luckcock, H.; Moss, I. black hole have skyrmion hair. *Phys. Lett. B* **1986**, *176*, 341–345. [[CrossRef](#)]
33. Droz, S.; Heusler, M.; Straumann, N. New black hole solutions with hair. *Phys. Lett. B* **1991**, *268*, 371–376. [[CrossRef](#)]
34. Bekenstein, J.D. Exact solutions of Einstein conformal scalar equations. *Ann. Phys.* **1974**, *82*, 535–547. [[CrossRef](#)]
35. Kanti, P.; Mavromatos, N.E.; Rizos, J.; Tamvakis, K.; Winstanley, E. Dilatonic black holes in higher curvature string gravity. *Phys. Rev. D* **1996**, *54*, 5049–5058. [[CrossRef](#)]
36. Mignemi, S.; Stewart, N.R. Charged black holes in effective string theory. *Phys. Rev. D* **1993**, *47*, 5259–5269.
37. Torii, T.; Yajima, H.; Maeda, K.-I. Dilatonic black holes with Gauss-Bonnet term. *Phys. Rev. D* **1997**, *55*, 739–753. [[CrossRef](#)]
38. Kleihaus, B.; Kunz, J.; Radu, E. Rotating Black Holes in Dilatonic Einstein-Gauss-Bonnet Theory. *Phys. Rev. Lett.* **2011**, *106*, 151104. [[CrossRef](#)]
39. Herdeiro, C.A.R.; Radu, E. Black hole scalarization from the breakdown of scale invariance. *Phys. Rev. D* **2019**, *99*, 084039. [[CrossRef](#)]
40. Antoniou, G.; Bakopoulos, A.; Kanti, P. Evasion of No-Hair Theorems and Novel Black-Hole Solutions in Gauss-Bonnet Theories. *Phys. Rev. Lett.* **2018**, *120*, 131102. [[CrossRef](#)]
41. Doneva, D.D.; Yazadjiev, S.S. New Gauss-Bonnet Black Holes with Curvature-Induced Scalarization in Extended Scalar-Tensor Theories. *Phys. Rev. Lett.* **2018**, *120*, 131103. [[CrossRef](#)] [[PubMed](#)]

42. Silva, H.O.; Sakstein, J.; Gualtieri, L.; Sotiriou, T.P.; Berti, E. Spontaneous scalarization of black holes and compact stars from a Gauss-Bonnet coupling. *Phys. Rev. Lett.* **2018**, *120*, 131104. [[CrossRef](#)] [[PubMed](#)]
43. Brihaye, Y.; Herdeiro, C.; Radu, E. The scalarised Schwarzschild-NUT spacetime. *Phys. Lett. B* **2019**, *788*, 295–301. [[CrossRef](#)]
44. Herdeiro, C.A.R.; Radu, E.; Sanchis-Gual, N.; Font, J.A. Spontaneous Scalarization of Charged Black Holes. *Phys. Rev. Lett.* **2018**, *121*, 101102. [[CrossRef](#)] [[PubMed](#)]
45. Johannsen, T.; Psaltis, D. Testing the No-Hair Theorem with Observations in the Electromagnetic Spectrum: II. Black-Hole Images. *Astrophys. J.* **2010**, *718*, 446–454. [[CrossRef](#)]
46. Broderick, A.E.; Johannsen, T.; Loeb, A.; Psaltis, D. Testing the No-Hair Theorem with Event Horizon Telescope Observations of Sagittarius A*. *Astrophys. J.* **2014**, *784*, 7. [[CrossRef](#)]
47. Cunha, P.V.P.; Herdeiro, C.A.R.; Radu, E.; Runarsson, H.F. Shadows of Kerr black holes with scalar hair. *Phys. Rev. Lett.* **2015**, *115*, 211102. [[CrossRef](#)]
48. Cunha, P.V.P.; Herdeiro, C.A.R.; Radu, E.; Runarsson, H.F. Shadows of Kerr black holes with and without scalar hair. *Int. J. Mod. Phys. D* **2016**, *25*, 1641021. [[CrossRef](#)]
49. Vincent, F.H.; Gourgoulhon, E.; Herdeiro, C.; Radu, E. Astrophysical imaging of Kerr black holes with scalar hair. *Phys. Rev. D* **2016**, *94*, 084045. [[CrossRef](#)]
50. Khodadi, M.; Allahyari, A.; Vagnozzi, S.; Mota, D.F. Black holes with scalar hair in light of the Event Horizon Telescope. *J. Cosmol. Astropart. Phys.* **2020**, *9*, 26. [[CrossRef](#)]
51. Afrin, M.; Kumar, R.; Ghosh, S.G. Parameter estimation of hairy Kerr black holes from its shadow and constraints from M87*. *Mon. Not. R. Astron. Soc.* **2021**, *504*, 5927–5940.
52. Afrin, M.; Ghosh, S.G. Testing Horndeski gravity from EHT observational results of rotating black holes. *Astrophys. J.* **2022**, *932*, 51. [[CrossRef](#)]
53. Gan, Q.; Wang, P.; Wu, H.; Yang, H. Photon ring and observational appearance of a hairy black hole. *Phys. Rev. D* **2021**, *104*, 044049. [[CrossRef](#)]
54. Gan, Q.; Wang, P.; Wu, H.; Yang, H. Photon spheres and spherical accretion image of a hairy black hole. *Phys. Rev. D* **2021**, *104*, 024003. [[CrossRef](#)]
55. Herdeiro, C.A.R.; Radu, E. Spherical electro-vacuum black holes with resonant, scalar Q -hair. *Eur. Phys. J. C* **2020**, *80*, 390. [[CrossRef](#)]
56. Hong, J.-P.; Suzuki, M.; Yamada, M. Spherically Symmetric Scalar Hair for Charged Black Holes. *Phys. Rev. Lett.* **2020**, *125*, 111104. [[CrossRef](#)]
57. Mai, Z.-F.; Yang, R.-Q. Stability analysis of a charged black hole with a nonlinear complex scalar field. *Phys. Rev. D* **2021**, *104*, 044008. [[CrossRef](#)]
58. Brihaye, Y.; C onsole, F.; Hartmann, B. Inflation inside non-topological defects and scalar black holes. *Symmetry* **2020**, *13*, 2. [[CrossRef](#)]
59. Dias, O.J.C.; Horowitz, G.T.; Santos, J.E. Inside an asymptotically flat hairy black hole. *J. High Energy Phys.* **2021**, *12*, 179. [[CrossRef](#)]
60. Zhang, S.-J. Spherical black holes with minimally coupled scalar cloud/hair in Einstein–Born–Infeld gravity. *Eur. Phys. J. C* **2022**, *82*, 501. [[CrossRef](#)]
61. Brihaye, Y.; Herdeiro, C.; Radu, E. $D = 5$ static, charged black holes, strings and rings with resonant, scalar Q -hair. *arXiv* **2022**, arXiv:2207.13114.
62. Devi, S.; Chakrabarti, S.; Majhi, B.R. Shadow of quantum extended Kruskal black hole and its super-radiance property. *arXiv* **2021**, arXiv:2105.11847.
63. Azreg-Ainou, M. Regular and conformal regular cores for static and rotating solutions. *Phys. Lett. B* **2014**, *730*, 95–98. [[CrossRef](#)]
64. Jusufi, K.; Azreg-Ainou, M.; Jamil, M.; Wei, S.-W.; Wu, Q.; Wang, A. Quasinormal modes, quasiperiodic oscillations, and the shadow of rotating regular black holes in nonminimally coupled Einstein–Yang–Mills theory. *Phys. Rev. D* **2021**, *103*, 024013.
65. Bambhaniya, P.; Verma, J.S.; Dey, D.; Joshi, P.S.; Joshi, A.B. Lense–Thirring effect and precession of timelike geodesics in slowly rotating black hole and naked singularity spacetimes. *arXiv* **2021**, arXiv:2109.11137.
66. Grandclement, P.; Novak, J. Spectral methods for numerical relativity. *Living Rev. Relativ.* **2009**, *12*, 1. [[CrossRef](#)]
67. Grienering, S. Holographic Quenches and Anomalous Transport. Master’s Thesis, Friedrich Schiller University Jena, Institute for Theoretical Physics, Jena, Germany, 2016.
68. Andrade, T. Holographic Lattices and Numerical Techniques. *arXiv* **2017**, arXiv:1712.00548.
69. Flory, M.; Grienering, S.; Morales-Tejera, S. Critical and near-critical relaxation of holographic superfluids. *arXiv* **2022**, arXiv:2209.09251.
70. Donos, A.; Gauntlett, J.P. Holographic Q -lattices. *J. High Energy Phys.* **2014**, *4*, 40. [[CrossRef](#)]
71. Ling, Y.; Liu, P.; Wu, J.-P.; Wu, M.-H. Holographic superconductor on a novel insulator. *Chin. Phys. C* **2018**, *42*, 013106. [[CrossRef](#)]
72. Ling, Y.; Liu, P.; Wu, M.-H. Holographic superconductor induced by charge density waves. *Phys. Rev. D* **2020**, *102*, 126013. [[CrossRef](#)]
73. Ling, Y.; Wu, M.-H. Holographic striped superconductor. *J. High Energy Phys.* **2021**, *3*, 260. [[CrossRef](#)]
74. Carter, B. Global structure of the Kerr family of gravitational fields. *Phys. Rev.* **1968**, *174*, 1559–1571. [[CrossRef](#)]
75. Wang, Y.; Sun, W.; Liu, F.; Wu, X. Construction of Explicit Symplectic Integrators in General Relativity. I. Schwarzschild Black Holes. *Astrophys. J.* **2021**, *907*, 66. [[CrossRef](#)]

76. Wang, Y.; Sun, W.; Liu, F.; Wu, X. Construction of Explicit Symplectic Integrators in General Relativity. II. Reissner–Nordström Black Holes. *Astrophys. J.* **2021**, *909*, 22. [[CrossRef](#)]
77. Wang, Y.; Sun, W.; Liu, F.; Wu, X. Construction of Explicit Symplectic Integrators in General Relativity. III. Reissner–Nordström–(anti)-de Sitter Black Holes. *Astrophys. J. Suppl.* **2021**, *254*, 8. [[CrossRef](#)]
78. Wu, X.; Wang, Y.; Sun, W.; Liu, F. Construction of Explicit Symplectic Integrators in General Relativity. IV. Kerr Black Holes. *Astrophys. J.* **2021**, *914*, 63. [[CrossRef](#)]
79. Luo, J.; Wu, X.; Huang, G.; Liu, F. Explicit Symplectic-like Integrators With Midpoint Permutations for Spinning Compact Binaries. *Astrophys. J.* **2017**, *834*, 64. [[CrossRef](#)]
80. Pan, G.; Wu, X.; Liang, E. Extended phase-space symplectic-like integrators for coherent post-Newtonian Euler-Lagrange equations. *Phys. Rev. D* **2021**, *104*, 044055. [[CrossRef](#)]
81. Zhong, S.-Y.; Wu, X.; Liu, S.-Q.; Deng, X.-F. Global symplectic structure-preserving integrators for spinning compact binaries. *Phys. Rev. D* **2010**, *82*, 124040. [[CrossRef](#)]
82. Mei, L.; Wu, X.; Liu, F. On preference of Yoshida construction over Forest-Ruth fourth-order symplectic algorithm. *Eur. Phys. J. C* **2013**, *73*, 2413. [[CrossRef](#)]
83. Bambi, C. *Black Holes: A Laboratory for Testing Strong Gravity*; Springer: Singapore, 2017.
84. Cunningham, C.T.; Bardeen, J.M. The optical appearance of a star orbiting an extreme Kerr black hole. *Astrophys. J. Lett.* **1972**, *173*, L137. [[CrossRef](#)]
85. Abdujabbarov, A.; Amir, M.; Ahmedov, B.; Ghosh, S.G. Shadow of rotating regular black holes. *Phys. Rev. D* **2016**, *93*, 104004. [[CrossRef](#)]
86. Zakharov, A.F. Constraints on a charge in the Reissner-Nordström metric for the black hole at the Galactic Center. *Phys. Rev. D* **2014**, *90*, 062007. [[CrossRef](#)]
87. Hioki, K.; Maeda, K.-I. Measurement of the Kerr Spin Parameter by Observation of a Compact Object's Shadow. *Phys. Rev. D* **2009**, *80*, 024042. [[CrossRef](#)]